Efficient fabrication of highly stretchable and ultrasensitive thermoplastic polyurethane/carbon nanotubes foam with anisotropic pore structures for human motion monitoring

*Qing-wen Yuan[a], Hao-wei Jiang[a], Tian-yuan Gao[a], Sen-hao Zhang[a], Shun-heng Jia[a], Ting Wu[*b], Jin-ping Qu[*a,b]*

[a]Guangdong Provincial Key Laboratory of Technique and Equipment for Macromolecular Advanced Manufacturing, National Engineering Research Center of Novel Equipment for Polymer Processing, Key Laboratory of Polymer Processing Engineering, Ministry of Education, South China University of Technology, Guangzhou, Guangdong, 510640, China.

[b]Key Laboratory of Material Chemistry for Energy Conversion and Storage, Ministry of Education, Hubei Key Laboratory of Material Chemistry and Service Failure and Hubei Engineering Research Center for Biomaterials and Medical Protective Materials, School of Chemistry and Chemical Engineering, Huazhong University of Science and Technology, Wuhan, Hubei, 430074, China.

---

[*] Corresponding author.
E-mail address: tingwu@hust.edu.cn (T. Wu).
E-mail address: jpqu@scut.edu.cn (J. P. Qu).

The porous strain sensor with copper electrodes is clamped by insulating fixtures, and the copper electrodes connected to the electrochemical workstation can move with the deformation of the sensor.
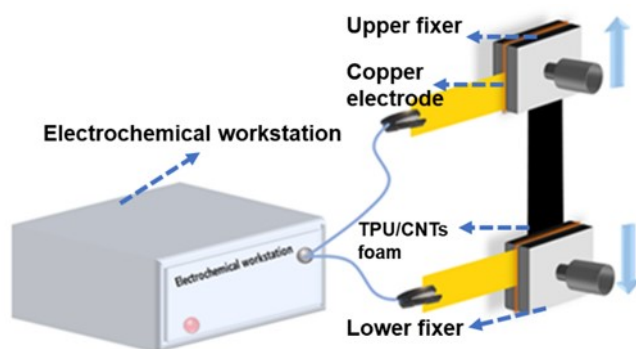

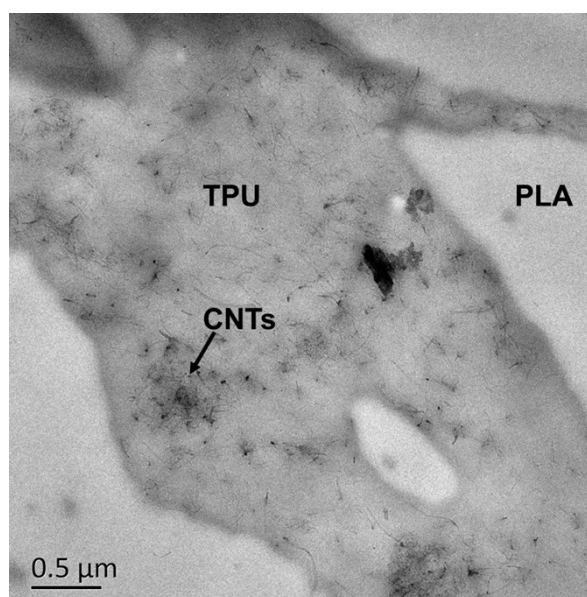**Fig. S1.** Schematic diagram of the measurement of the resistance during stretching.

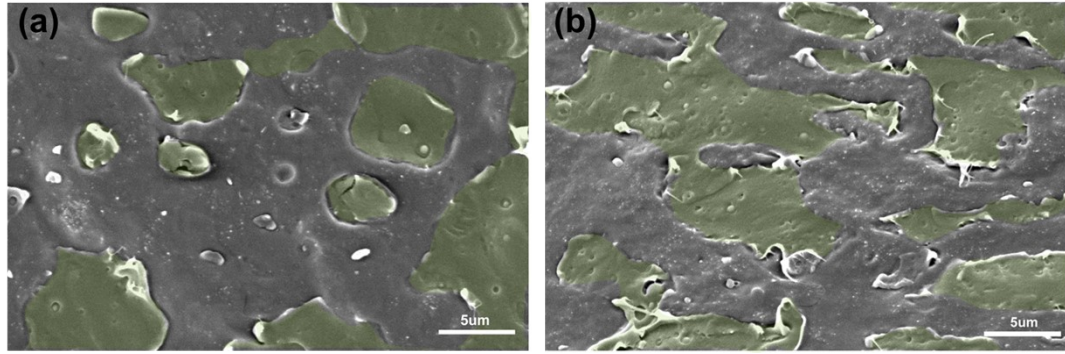**Fig. S2.** TEM images of TPU/PLA/CNTs composites with 1.5wt%.

Fig. S3. SEM images of TPU/PLA/CNTs composites with (a)0.5 wt%, (b)3 wt%.
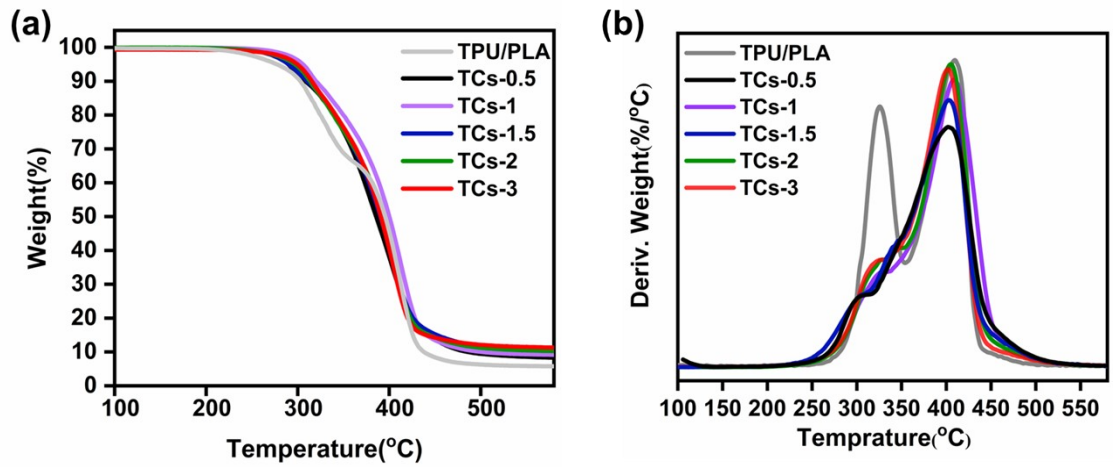

Fig. S4. (a) TGA and (b) DTGA curves of TPU/PLA, TPU/CNTs foams with 0.5wt%,
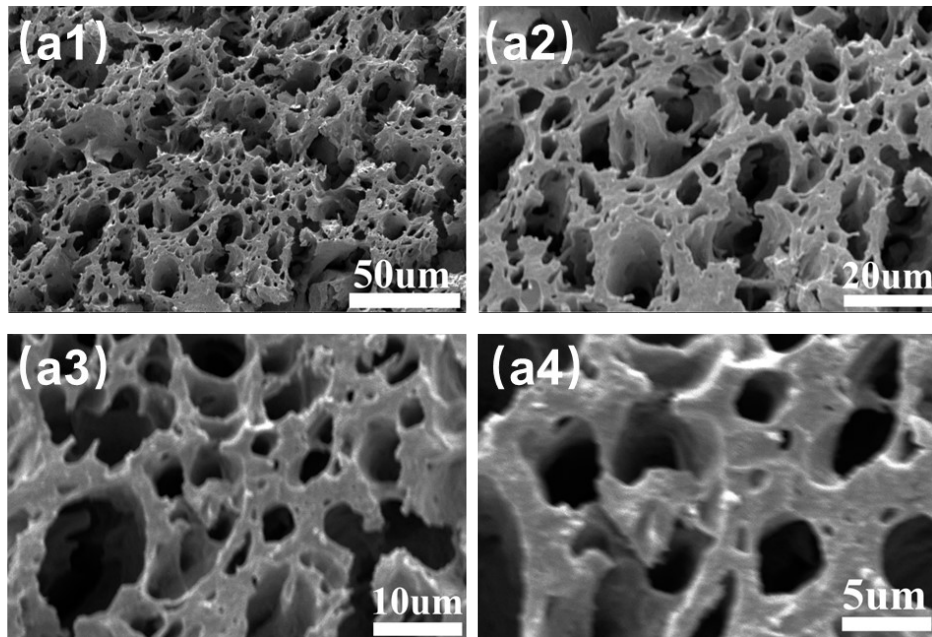
1wt%, 1.5wt%, 2wt%, 3wt% CNTs.

Fig. S5. The cryo-fracture of TCs-3 foam along the perpendicular direction.

As shown in **Fig. S6a**, the CBER is comprised of two co-biaxial eccentric rotors and a stator. The inner cavity of the stator presents "8"-shape formed by two intersecting cylindrical surfaces. The two rotors are installed in the inner cavity of the stator, and they mesh with each other and have the same rotation direction. **Fig. S6a** also shows the different positions of the rotors and the spatial variation of the stator cavity in a period. From time t_0 to time $t_0+T/4$, the mixing chamber is divided into two chambers of different sizes by rotors and stator, wherein the upper chamber is smaller than the lower one. At time $t_0+3T/8$, two chambers of different sizes connect into one chamber. From time $t_0+T/2$ to time $t_0+3T/4$, the mixing chamber is divided into two chambers with different sizes once again, but the upper chamber is larger than the lower one. At time $t_0+7T/8$, the second connection of the two chambers happens. Therefore, the shape of both chambers is changing during the rotation process of the rotors, and the single chamber undergoes two compression-release cycles in one period. Consequently, the materials between the stator and the eccentric rotors undergoing four chamber-to-chamber exchanges receive pulsed volume deformation when periodically compressed and released, thus completing the plasticizing and mixing process dominated by the elongation flow. **Fig. S6b** shows the mixing and dispersing mechanism PLA and CNTs under the extensional flow field inside a CBER equipment. During the convergent region，PLA phase is stretched and compressed under the elongational flow field caused by the volume change of the chamber. Then, the deformed PLA phase is dispersed in the TPU matrix after breaking when entering the divergent region. In addition, CNTs are uniformly dispersed in the TPU matrix with melt in the normal

stress field generated by the extensional flow field. Detailed information has been added in the revised supplementary material.
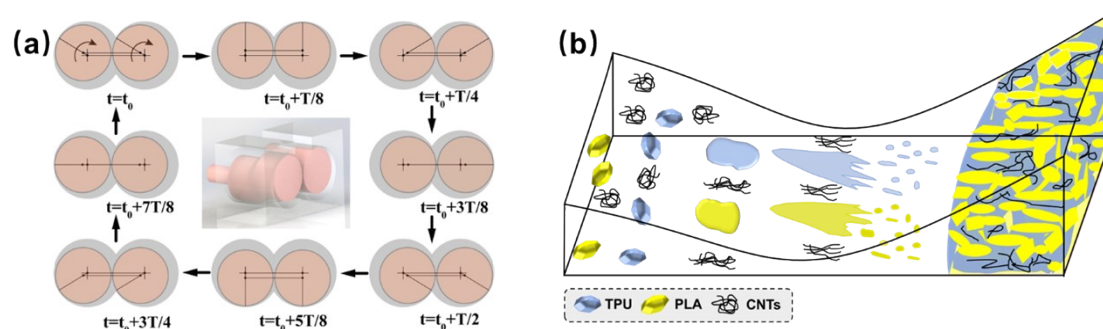

Fig. S6. (a) The relative location of the rotor at different times. (b) Schematic diagram of mixing and dispersing mechanism under the leading action of the volumetric extensional flow field.
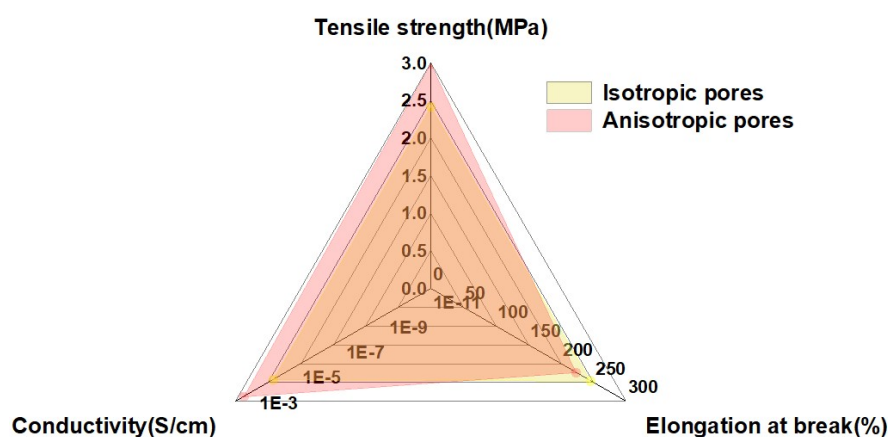

Fig. S7. The comparison of electrical and mechanical properties between the isotropic pores and anisotropic pores.

Fig. S8a and **Fig. S8b** show the sensing characteristics of the x and y direction of anisotropic pores, and $\Delta R/R_0$ increases with the increasing strain because of the disconnection of conductive pathways. In the x direction of the anisotropic pores, GFs are 16.47, 99.73, 373.96, and 1189.19 in the strain range of 0 ~ 100%, 100 ~ 160%, 160 ~ 200%, and 200 ~ 221%, respectively. However, in the y direction, GFs are 9.18,

31.68, 103.86, and 323.63 in the strain range of 0 ∼ 100%, 100 ∼ 200%, 200 ∼ 280%,

and 280 ∼ 325%, respectively, indicating that the sensitivity of the perpendicular

direction is lower than that of the parallel direction. **Fig. S8c** shows the sensing

characteristics of the z direction of anisotropic pores. $\Delta R/R_0$ decreases with the

increasing compressive strain because of the increase in conductive pathways. It is

worth noting that the decreasing $\Delta R/R_0$ with strain is nonlinear, thus GFs change with

the strain. At the strain range of 0 ∼ 58%, $\Delta R/R_0$ has a prominent decrease because the

deformation of the pores promotes the compaction of the segregated CNTs network to

form conductive pathways, which leads to the GF of 1.38. At the strain range of 58 ∼

74%, the pores are almost compressed to flat, which is difficult to cause the increase of

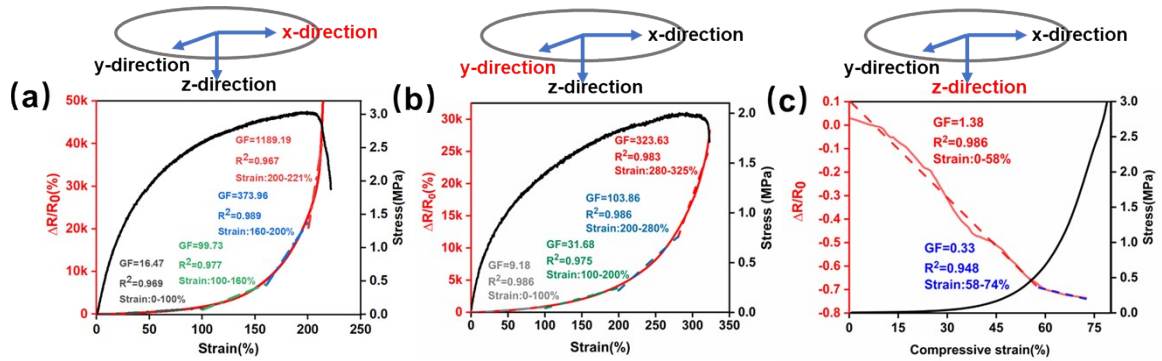conductive pathways, so GF is 0.33.

Fig. S8. The sensing behavior of TCs-3 foam along (a) the x-direction of anisotropic

pores, (b) the y-direction of anisotropic pores, (c) the z-direction of anisotropic pores.
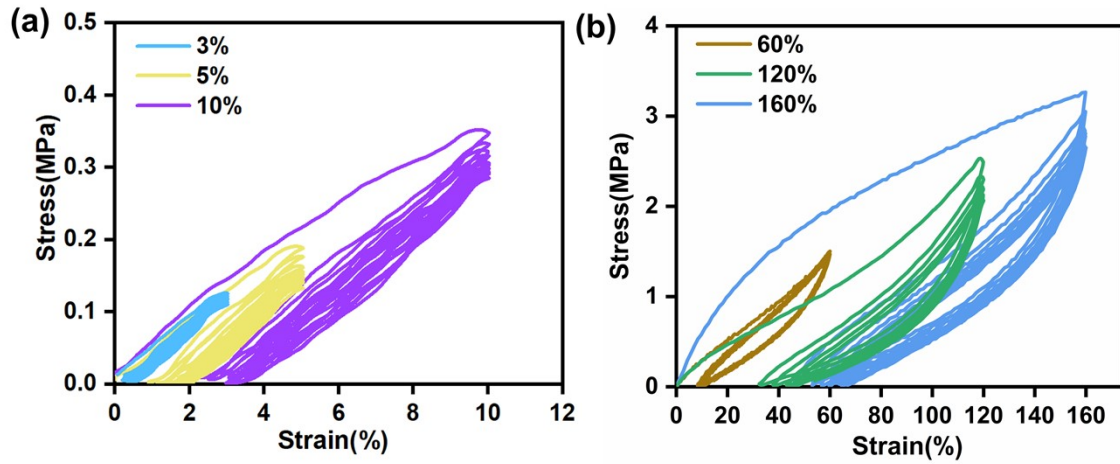
Fig. S9. Stress-strain curves of porous TCs-3 foam during stretching-releasing at (a) 3%, 5%, 10%. (b) 60%, 120%, 160%.

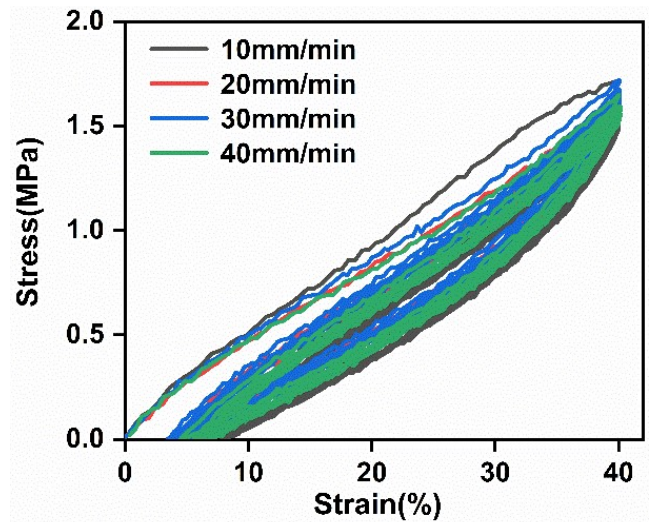**Fig. S10.** Stress-strain curves of porous TCs-3 foam during stretching-releasing at 40% with different tensile speed.

Table S1. Surface energy data of components

Component	γ^p (mJ/m²)	γ^d (mJ/m²)	γ (mJ/m²)
PLA	5.43	35.59	41.02
TPU	4.30	28.29	32.59
CNT	10.2	17.6	27.8

$$\gamma = \gamma^d + \gamma^p \qquad \backslash\text{* MERGEFORMAT (1)}$$

Table S2. Interfacial energy as calculated by Harmonic-mean and Geometric-mean equations

Samples	Based on Harmonic-mean equation(mJ/m^2)	Based on Geometric-mean equation(mJ/m^2)
PLA/TPU	0.97	0.48
PLA/CNT	7.54	3.88
TPU/CNT	4.89	2.52

$$\gamma = \gamma^d + \gamma^p \qquad \text{\textbackslash* MERGEFORMAT (2)}$$

Harmonic-mean equation:

$$\gamma_{12} = \gamma_1 + \gamma_2 - 4\left(\frac{\gamma_1^d \gamma_2^d}{\gamma_1^d + \gamma_2^d} + \frac{\gamma_1^p \gamma_2^p}{\gamma_1^p + \gamma_2^p} \right) \qquad \text{\textbackslash* MERGEFORMAT (3)}$$

Geometric-mean equation:

$$\gamma_{12} = \gamma_1 + \gamma_2 - 2\left(\sqrt{\gamma_1^d \gamma_2^d} + \sqrt{\gamma_1^p \gamma_2^p} \right) \qquad \text{\textbackslash* MERGEFORMAT (4)}$$

Where γ_1, γ_2 is the surface energy of polymer1 and polymer2, respectively, $\gamma_1^d, \gamma_1^p, \gamma_2^d, \gamma_2^p$ are the dispersive and polar parts of the surface energy of component1 and component 2, respectively.

$$\omega_a = \frac{\gamma_{PLA-CNTs} - \gamma_{TPU-CNTs}}{\gamma_{PLA-TPU}} \qquad \text{\textbackslash* MERGEFORMAT (5)}$$

The interfacial energies between nanofiller and polymer 1, between nanofiller and polymer 2, and between the two phases. If $\omega_a > 1$, the nanofiller preferentially locates in polymer 2; if $\omega_a < -1$, the nanofiller preferentially locates in polymer 1, and if $-1 < \omega_a < 1$, the nanofiller locates at the interface between the two phases. According to Equation (5), the wetting coefficient was calculated as 2.73 and 2.83 based Harmonic-mean equation and Geometric-mean equation, respectively, indicating that CNTs are located in the TPU phase preferentially.